International Conference on Space Optics—ICSO 2022

Dubrovnik, Croatia

3–7 October 2022

Edited by Kyriaki Minoglou, Nikos Karafolas, and Bruno Cugny,

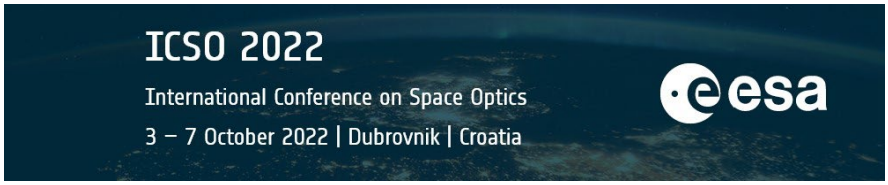

Results of the METimage HgCdTe flight photodetector test campaign

International Conference on Space Optics — ICSO 2022, edited by Kyriaki Minoglou, Nikos Karafolas, Bruno Cugny, Proc. of SPIE Vol. 12777, 127773R · © 2023 ESA and CNES · 0277-786X · doi: 10.1117/12.2690563

Results of the METimage HgCdTe flight photodetector test campaign

Rémi Rivière*[1], Klaus-Werner Kruse[2], Henrique Candeias[1], Laurent Vial[3], Céline Riuné[3], Michael Skegg[1], Olivier Saint-Pé[4]
[1]Airbus Defence and Space GmbH, Robert-Koch-Str. 1, 82024 Taufkirchen, Germany
[2]Airbus Defence and Space GmbH, Claude-Dornier-Str., 88090 Immenstaad, Germany
[3]LYNRED, 364 av. de Valence, 38113 Veurey-Voroize, France
[4]Airbus Defence and Space SAS, 31 rue des Cosmonautes, 31400 Toulouse, France
*remi.riviere@airbus.com

ABSTRACT

The METimage instrument is an Airbus-primed passive superspectral imaging radiometer measuring thermal radiance emitted by the Earth and solar backscattered radiation in 20 spectral channels from 0.44µm to 13.35µm. The instrument achieves the entire Earth coverage at a low-Earth polar-orbit on daily basis by constantly scanning with spatial resolution of 500m at nadir and constant spatial sampling angle (SSA) across a 2670km swath. In the thermal domain, the most crucial part of the system is the pair of cryogenically-cooled HgCdTe (MCT) photodetectors intended for thermal-domain SMWIR and LVWIR, the development and manufacturing of which was contracted to LYNRED, who have successfully delivered the flight models to Airbus. In this work, the results of the Airbus-hosted flight detection-chain level test campaign in nominal vacuum and cryogenic environment are presented. Their system impacts are evaluated to conclude the expected full flight-worthiness of both delivered photodetectors into the METimage optical payload. First, both dark currents and offsets are characterized: both parameter noise levels quantitatively outperform their predicted values, minimizing their impact on the system signal-to-noise ratio (SNR). Then the response linearity of both photodetectors over the required thermal radiance ranges has been measured and has shown better performances than predicted by design over the setup-accessible solar and 185K to 280K thermal radiance ranges. Finally, the random telegraph signal (RTS) signature of both photodetectors is thoroughly characterized based on a novel sharp-edge detection method in conditions mimicking in-orbit operation: after periodic cooldowns and at stable nominal temperatures. Based on these measurements, the sub-pixel selection map (SPSM) is generated, enabling to deselect image elements that are deemed to degrade overall performance from a system perspective. Thanks to a demanding flight model selection procedure applied by LYNRED, the RTS test results of the sorted out devices are significantly better than expected, hence ensuring compliance for system SNR and homogeneity. Full flight worthiness is therefore confirmed and final integration of both photodetectors in the first METimage flight instrument optical system is currently ongoing.

Keywords: METimage, thermal infrared, HgCdTe (MCT), non-linearity, random telegraph signal (RTS)

1. INTRODUCTION

1.1 The Metimage optical instrument

The METimage instrument is an Airbus-primed passive superspectral imaging radiometer measuring thermal radiance emitted by the Earth and solar backscattered radiation in 20 spectral channels from 0.44µm to 13.35µm. The instrument achieves the entire Earth coverage at a low-Earth polar-orbit on daily basis by constantly whisk-broom-scanning with spatial resolution of 500m at nadir and constant spatial sampling angle (SSA) across a 2670km swath. Architecturally [1][2], this instrument consists in a reflective telescope imaging ground samples to a first focal plane where they are spectrally separated into SMWIR and LVWIR channels from 1.24µm to 13.35µm. These channels are then reimaged using cold refractive optics onto a pair of cryogenically-cooled HgCdTe (MCT) photodetectors, one for each spectral domain SMWIR and LVWIR. Their development and manufacturing have been contracted to LYNRED, who have successfully delivered the flight models to Airbus. Importantly, each spatial sample or macro-pixel (MP) is imaged on 3x3 readout pixels (ROP) of 90x90µm², each ROP being made of 3x3 sub-pixel (SP) of 30x30µm² that can be enabled individually. Spatial samples are acquired every 218µs with an integration time of 203µs.

1.2 Campaign objective

To achieve early characterization and calibration [3], both flight model detectors delivered by LYNRED are subjected to a thorough test campaign at Airbus premises to confirm their flight-worthiness w.r.t to their predicted modelled performances or performance allocations. The results of this campaign are the subject of the work presented here.

1.3 Experimental setup

Both detectors are assembled with their flight imaging optics, cold aperture stops, channel-separating spectral filters and field stops. They are then placed in a dedicated cryostat thermostating the whole assembly at representative vacuum pressure and operational temperatures, notably 58+-/1K for both detectors. Importantly, both detectors are paired with their flight supply and readout electronics, ensuring relevant detection chain in-orbit representativity of this cryogenic imaging assembly (CIA). The illumination of the object focal plane is ensured by a diffused 2000K incandescent lamp for the SWIR, corresponding to solar channels, while thermal channels MWIR and LVWIR are illuminated by a > 0.98 emissivity black body which is thermally tunable between 185K and 350K. Note that étendue matching is achieved with proper baffling. Finally, both illuminators can be blocked with cold mechanical shutters to ensure dark condition.

2. EXPERIMENTAL RESULTS

2.1 Dark current

Both detectors dark currents are quantified by measuring their response to dark condition at increasing integration times. For the SMWIR detector, dark current values are larger than those predicted from only the detector, but still > 1 order of magnitude lower than predicted dark response combining both detector dark currents and test setup thermal background. Moreover, as shown in Fig. 1, the measured detector response does not vary with detector temperature, hence proving that the measured signal is dominated by thermal background, not by detector properties.

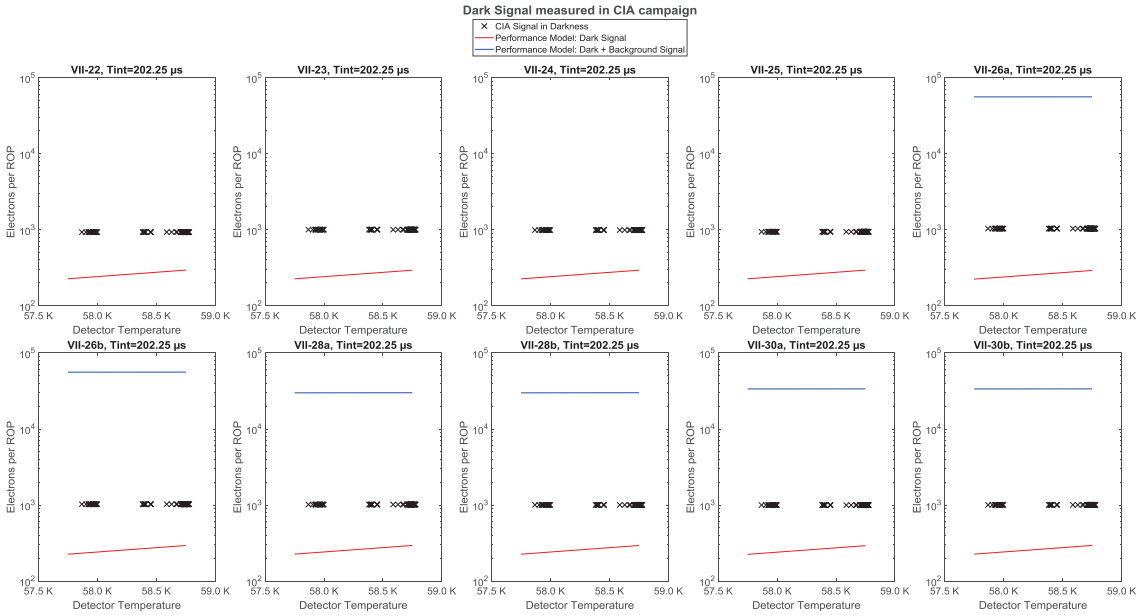

Figure 1. SMWIR detector dark response for varying detector temperatures and compared to the predicted detector and overall dark signals.

For the LVWIR detector on the contrary, measured values are slightly higher but close to predictions from detector only, as shown in Fig. 2. Here, the dark response increase with temperature proves that the measurement is dominated by the detector response. The systematic 15% to 20% overestimation is expected to come from the different operating detector temperatures between the Airbus and the LYNRED campaigns, the latter being the input for the shown model. Discrepancies between channels VII-40a and VII-40b possibly originates from differentiated SP selection patterns.

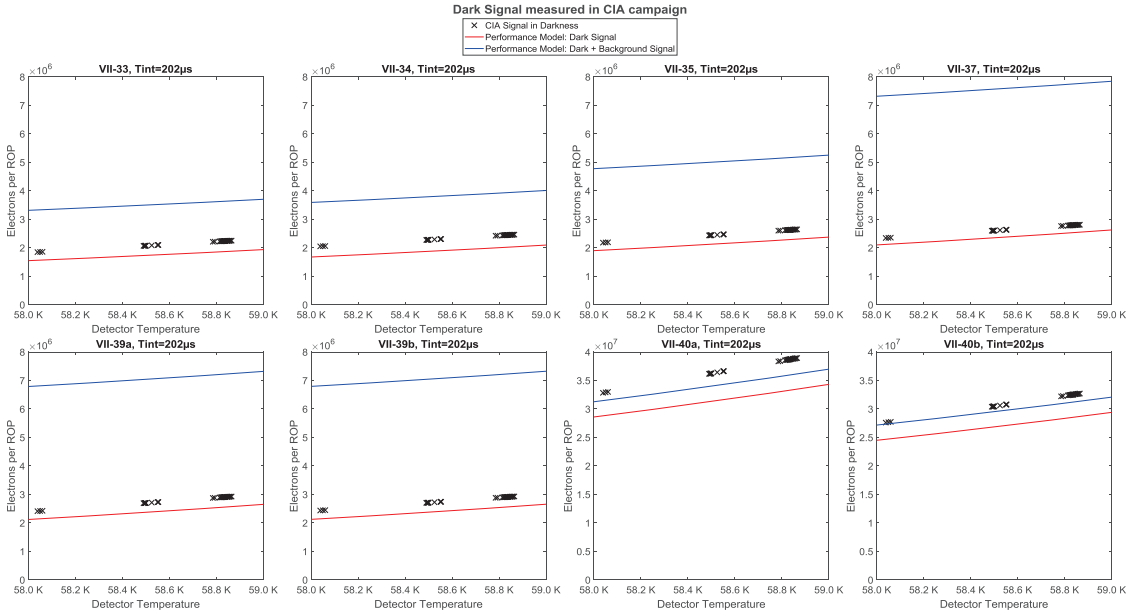

Figure 2. LVWIR detector dark response for varying detector temperatures and compared to the predicted detector and overall dark signals.

2.2 Offset and readout noise

Offsets, and more importantly readout noises (RON), are measured by recording long time series in dark condition at the nominal integration time. This enables to infer the total detector noise, i.e. the standard deviation of the signal both at MP and ROP level. Then, the dark signal shot noise is subtracted for both cases based on results from 2.1 to quantify the MP and ROP RON. Both results are then combined to extract pixel-correlated and -uncorrelated parts of the RON.

The correlation to the predicted performance model is then verified by analyzing the contribution of SP into correlated and uncorrelated parts of the RON and comparing it to the model provided by LYNRED, as shown in the next 2 figures.

For SMWIR, the comparison is shown in Fig. 3. As expected, correlated noise does not vary with the number of selected SP while uncorrelated noise does. Agreement for both noises is proven, and after removing statistical outliers, most pixels outperform the predicted model while worst cases degrade it marginally by 3%. Hence, the flight SMWIR detector contribution to Metimage system statistical error performance is considered compliant.

Then, for LVWIR, the comparison is shown in Fig. 4. While the correlated noise behave as expected, uncorrelated noise slightly diverges from the predicted model at low SP number, leading to a minor performance degradation at low SP number, as high SP number correlated noise still outperform the predictions. Because of this, worst cases lead to a maximum of 15% performance degradation, still well within the performance contingency planned by Airbus. Hence, the flight LVWIR detector contribution to Metimage system statistical error performance is also considered compliant.

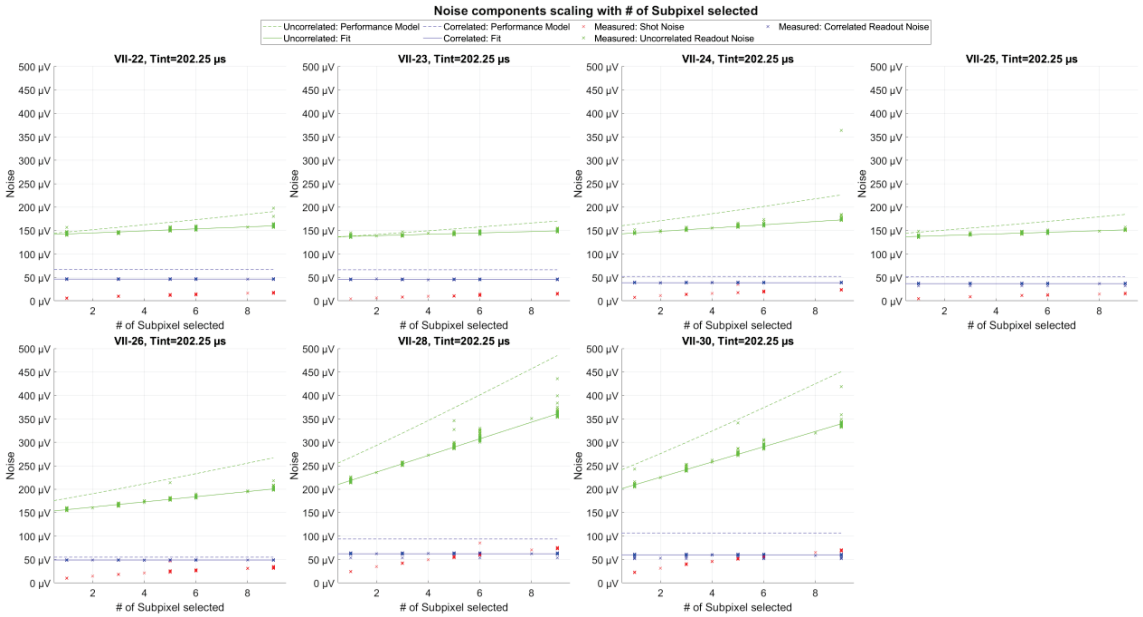

Figure 3. SMWIR detector noise contributors scaling with SP and compared to the predicted performance model.

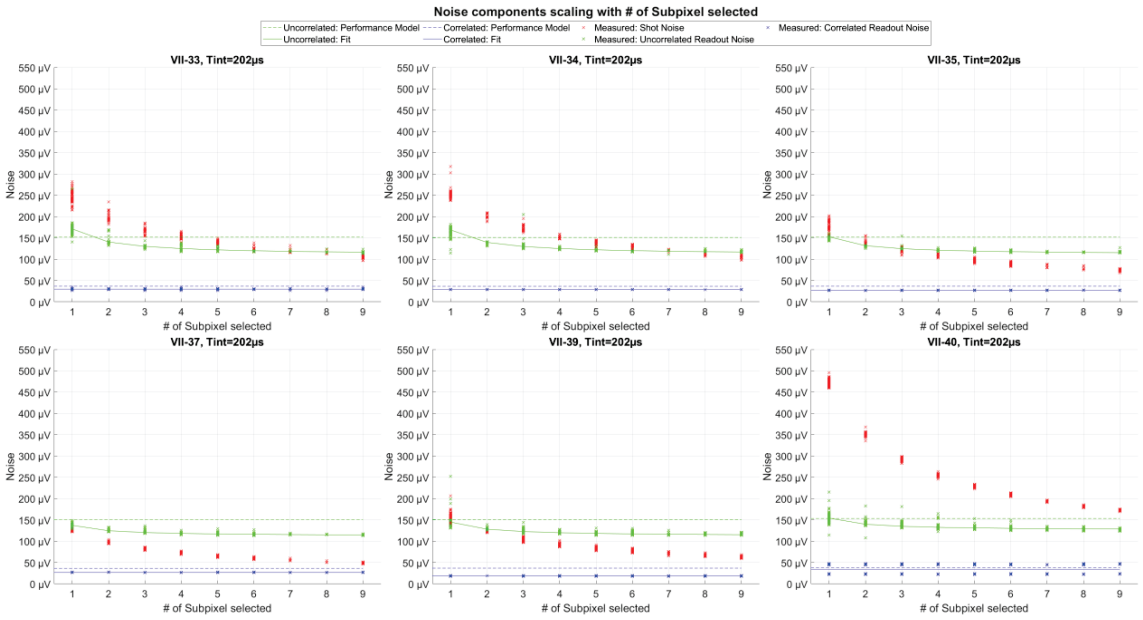

Figure 4. LVWIR detector noise contributors scaling with SP and compared to the predicted performance model.

2.3 Non-linearity

Because of the different aspects of the experimental setup used, solar (SWIR, 1.24-2.25µm) and thermal (MWIR, 3.74-4.05µm and LVWIR, 6.73-13.35µm) channels non-linearities are treated separately.

SWIR

To avoid experimental bias coming from the spectral instability of the 2000K incandescent source and from the intrinsic non-linearity of the filtered reference photodetector of the setup, non-linearity is inferred here from detector signals recording for varying integration times, for some different source fluxes. Additionally, dark pixel signals are subtracted from the illuminated ones to remove detrimental offset drifts. Indeed, the image of the field stop to the focal plane leave pixels not illuminated, hence providing a convenient dark reference. Finally, short integration times < 80µs are avoided as they introduce also a minor non-linearity.

Fig. 5 depicts an exemplary result for channel VII-25: on the top left, an example for 1 detector response for 1 flux level for varying integration time is shown, the abscissa ROP readout being the product of the recorded flux and the integration time. From all response curves at different fluxes, a linear fit is performed. The fit residues from flux and integration times are shown on the right top and bottom plots, respectively. Importantly however, the overall linear fit residuals is shown on the bottom left, the predicted radiance range over which the optical instrument is supposed to be compliant being colored in light purple. Over this range, residuals are sliced over 5% bins, averaged and the overall maximum is taken as the non-linearity figure of merit, here 0.14% for this channel.

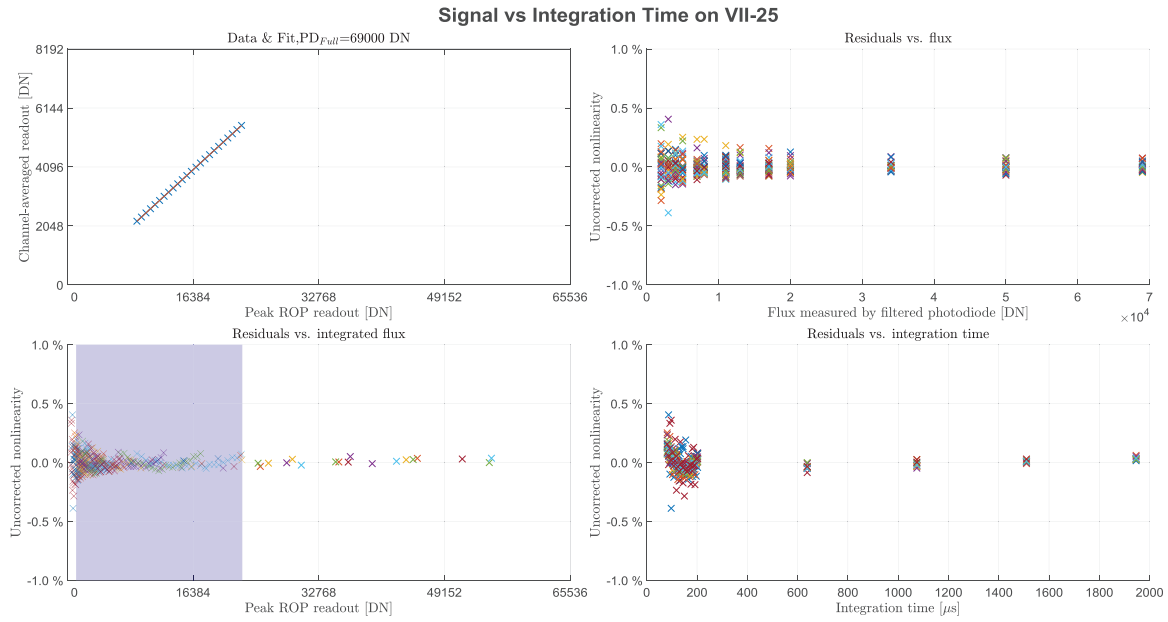

Figure 5. SWIR Channel VII-25 (2.25µm) non-linearity results. Top left: response vs flux at 1 integration time. Top right, bottom right, bottom left: Residuals from linearity for varying fluxes, integration times and the combination thereof, respectively.

For concision, plots for all channels are not shown it but their figures of merit are summarized in Table 1. Since an allocation of 0.10% was apportioned, most channels are indeed compliant. The marginal deviation for channel VII-25 was already known and still largely within the Airbus contingency. All these results are without any non-linearity corrections, hence stressing the exceptional quality of the detector delivered by LYNRED. Cumbersome operational post-processing is therefore here not necessary.

Table 1. SWIR achieved linearity accuracies.

Channel	VII-22	VII-23	VII-24	VII-25	Alloc.
Accuracy (%)	0.09	0.10	0.09	0.14	0.10

MWIR and LVWIR

For obvious background saturation reasons, the non-linearity here is only performed by varying the black body temperature from 185K to 350K. Unfortunately, above 280K the black body is suffering detrimental temperature instabilities, corrupting measurements. Hence, the evaluation of linearity of the detector is restricted to 185K to 280K, which is deemed sufficient to give a representative picture of the detector's quality.

To process the data from the thermal sweep, the conversion from black body temperature to optical flux within each channel's filter is performed using the predicted spectral response shape of the optical components from the CIA listed in 1.3. From this, it appears however that inter-channel cross-talk also introduces an extra non-linearity. Hence, the initially devised 5th-order polynomial used for correction is discarded and the uncorrected non-linearity residuals are simply used for performance evaluation.

Fig. 6 shows an exemplary result for channel VII-33 (6.73µm): from the linear fit residuals (bottom), histograms from uncorrected and 5th-order polynomial corrected residuals are depicted, for full and restricted ranges (middle and bottom, respectively). Here, the standard deviation of the restricted range and uncorrected residuals is taken as the figure of merit for each channel.

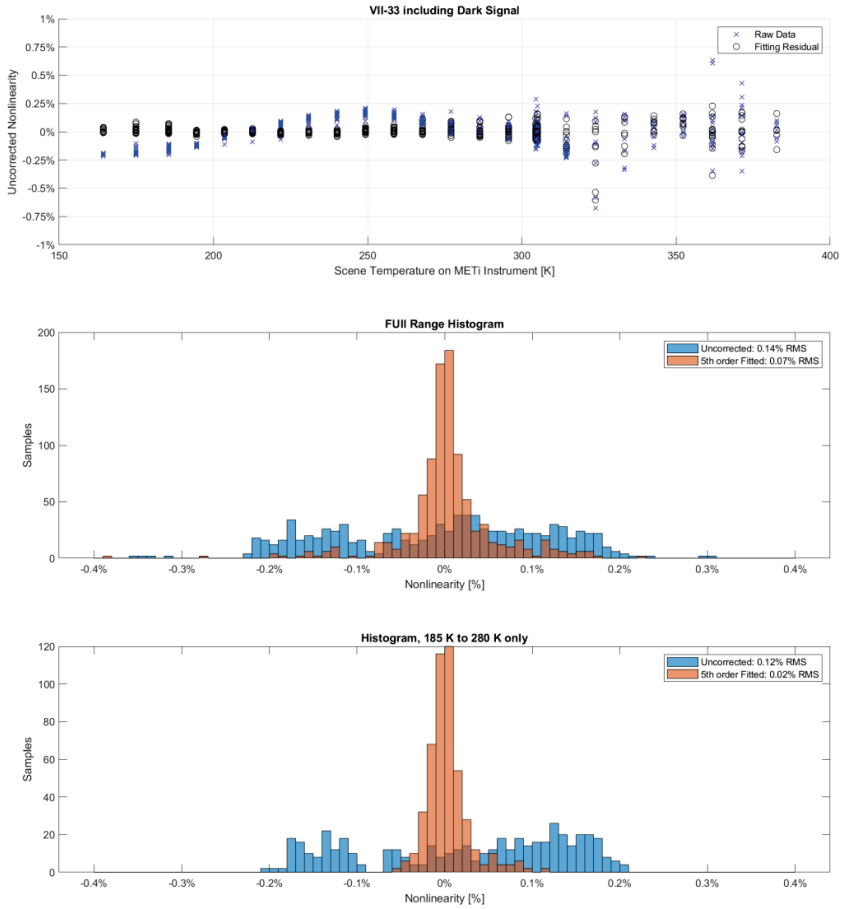

Figure 6. LVWIR Channel VII-33 (6.73µm) non-linearity results. Top: residuals from linearity fit over a larger thermal range. Middle: residual histogram. Bottom: residual histogram over the restricted 185K – 280K range.

For concision, plots for all channels are not shown it but their figures of merit without any correction are summarized in Table 2. Notably, like for the SWIR case, most channels achieve compliance < 0.10% accuracy without any correction,

the marginal non-compliance of channel VII-33 being well within the planned contingency. Similarly, with the obtained results the inter-channel and inter-spatial radiometric inhomogeneity has been also evaluated to be compliant to the predicted allocation. Like for the SWIR case, the detectors delivered by LYNRED are deemed compliant w.r.t to non-linearity, confirming its compliant integration into the Metimage optical instrument.

Table 2. LVWIR achieved linearity accuracies on the restricted range 1805K to 280K.

Channel	VII-26	VII-28	VII-30	VII-33	VII-34	VII-35	VII-37	VII-39	VII-40	Alloc.
Accuracy (%)	0.04	0.07	0.07	0.12	0.06	0.08	0.05	0.04	0.01	0.10

2.4 Random telegraph signals

RTS are sudden, brief and temporary jumps of dark signals, as depicted in Fig. 7. Here, instead of defining a jump height detrimental to the Metimage performances, the commonly agreed jump criterion from [4] applied to long dark time series [5] is used, and the pixel is flagged as a RTS pixel. In detail, a dark signal jump is flagged as RTS if its height H exceeds $\frac{2}{\sqrt{3}}\sigma_{ch}$, where σ_{ch} is the average of the channel noise standard deviation. Algorithmically here, the reliable and time-efficient edge detection technique detailed in [4] is applied as an industry standard. Note however that outperforming methods using artificial intelligence are also being investigated [6] at Airbus. After the flag procedure is applied to all pixels, an SPSM is generated and its impact to system performance is evaluated: for both detectors here, the final SPSM is described in 2.5.

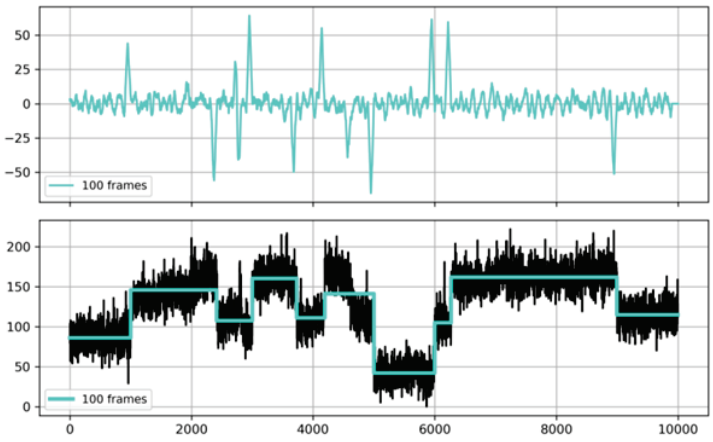

Figure 7. Experimental example of raw RTS jumps (bottom) and corresponding edge detection (top), at nominal t_{int}.

Importantly here, RTS mapping is performed after each thermal cycle the detectors are subjected to. Indeed, RTS maps partially change and it is crucial to generate a new SPSM each time thermal conditions are changed. Note however that it has been checked that this does not impact the system performances.

2.5 Sub-pixel selection maps

Finally, based on the previous results, a SPSM is generated, deselecting SPs with any of the following criteria:

- Excessive offset
- Excessive RON
- RTS flag
- Strongly reduced photoresponse
- Outlying gain compared the gain of SPs from the same ROP

The resulting SPSMs are shown in Fig. 8 for criterion values complying with the performance model. For both detectors, enough SPs remained to ensure system performance compliance, hence confirming the compliant integration of both detectors into the Metimage instrument.

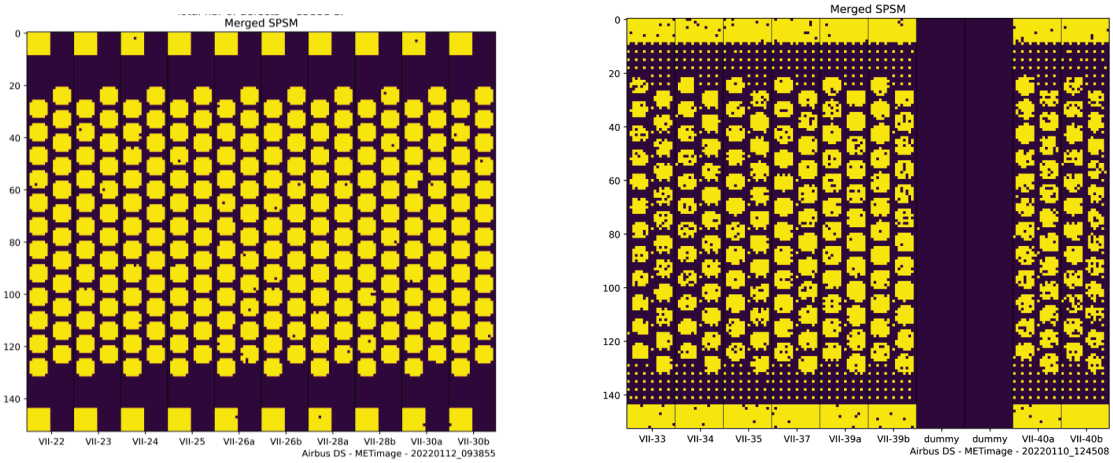

Figure 8. Final SPSM for SMWIR (left) and LVWIR (right). Yellow: selected, purple: deselected. Out-of-field pixels are also colored like the deselected ones.

3. CONCLUSION

Both flight models SMWIR and LVWIR MCT detectors delivered by LYNRED to Airbus have been subjected to a complete test campaign at Airbus premises. Charaterization under full in-orbit representativity has unambiguously confirmed the compliance of both delivered detectors and their flight-worthiness. Thanks to LYNRED demanding flight-model selection procedure at LYNRED for RTS for example, as well as a precise pre-characterization there, all measured characteristics have proven to be according or close to their modelled values. Propagation to the Metimage system performance model has been performed, detector contributions to system compliance has been verified, enabling Airbus to grant full flight-worthiness, from a system perspective. This milestone being completed, both detectors are now being integrated into the Metimage 1st flight model optical instrument.

REFERENCES

[1] Pellegrini G., “Optical design, challenges and development of the METimage instrument,” Proc. SPIE 11852, International Conference on Space Optics - ICSO 2020, 118520P, (2021).
[2] Wallner, O., Ergenzinger, K., Schmülling, F., Rivière, R., ICSO 2022 (2022).
[3] Rivière, R. Gnata, X., Coatantiec, C., Schmid, S., Albano, F., Bi, T., Del’haye, P., Burikova, T., Sacchetto, D., Stroganov, A., Geiselmann, M., Paus, S., „Space spectrograph design to calibration“, Proc. SPIE 11852, International Conference on Space Optics ICSO 2020, 118524A, (2021).
[4] Goiffon, G. R. Hopkinson, P. Magnan, F. Bernard, G. Rolland and O. Saint-Pé, "Multilevel RTS in Proton Irradiated CMOS Image Sensors Manufactured in a Deep Submicron Technology," IEEE Transactions on Nuclear Science, vol. 56, no. 4, pp. 2132-2141(2009).
[5] Candeias, H., Gnata, X., Harlander, M., Hermsen, M., Hohn, R., Riedl, S., Skegg, M., Williges, C., Reulke, R., "RTS effect detection in Sentinel-4 data," Proc. SPIE 10402, Earth Observing Systems XXII, 104021B, (2017).
[6] Ferrato M., Rivière R., Candeias H., Schmid S., Krauser J.,“ Space Optics Instrument Optimization and Characterization with Artificial Intelligence,” Proc. SPIE 11852, International Conference on Space Optics ICSO 2020, 1185265 (2021).